15

MIMO Vibration Control for a Flexible Rail Car Body: Design and Experimental Validation

Alexander Schirrer[1], Martin Kozek[1] and Jürgen Schöftner[2]
[1]*Institute of Mechanics and Mechatronics, Vienna University of Technology*
[2]*Institute of Technical Mechanics (ACCM), Johannes Kepler University of Linz*
Austria

1. Introduction

Car bodies of modern rail vehicles are designed as lightweight structures with the aim to minimize mass and thus operational energy demand. The central structural design requirements are given by the main static and dynamic loads. However, ride comfort becomes an increasingly important issue because the softer, more compliant structure exhibits low eigenfrequencies that significantly affect perceived passenger ride comfort.

Various approaches have been taken to reduce comfort-relevant vibrations of the car body that can be grouped into vibration isolation and vibration damping approaches. The isolation approaches include passive, semi-active, and active concepts to decouple the car body from the bogeys and wheel sets. The active approaches are more complex and can affect the safety against derailment, but potentially lead to improved isolation performance over their passive counterparts (see Foo & Goodall (2000) and Stribersky et al. (1998)).

The complementary vibration damping approaches intend to increase the elastic eigenmodes' damping ratios. A passive approach is taken in Hansson et al. (2004), active control schemes have been proposed in Kamada et al. (2005) as well as Schandl et al. (2007) and Benatzky (2006). The latter two references treat the same metro configuration and actuation concept as the present work.

This chapter presents LQG and weighted $\mathcal{H}_2$ MIMO control design methods for the vibration control of lightweight rail car body structures. These designs are studied and compared to achieve vibration reduction and passenger ride comfort improvement in a highly flexible metro rail car body. The metro car body structure is directly actuated via locally mounted Piezo stack actuators. Utilizing strain measurement signals, the control law actuates the structure with the aim of minimizing ride comfort-relevant acceleration signals across the car body interior. This system is subject to variations in damping and frequency of the flexible modes which pose a challenge for control design; the two control methods are implemented in a simulation as well as in a scaled experimental setup and their capabilities are investigated.

The work is embedded in a rich series of research and publications treating various aspects of control design for flexible rail car bodies. A robust $\mathcal{H}_\infty$-optimal control approach is surveyed in Kozek et al. (2011), including an overview on modeling, control design, simulation, identification, and experimental results. These research topics are focused on and detailed in Benatzky & Kozek (2005; 2007a;b); Benatzky et al. (2006; 2007); Bilik et al. (2006);

Popprath et al. (2006; 2007) and Schirrer et al. (2008). Further studies focus on Piezo stack actuators, their modeling and control (Schirrer, Kozek & Benatzky, 2008). Schirrer & Kozek (2008) and Schirrer (2010) report co-simulation studies of the multi-body system dynamics, the control law, and a non-linear actuator model. The underlying research project and its results are documented in two doctorate theses (Benatzky, 2006; Schandl, 2005), as well as in a series of master / diploma theses (Bilik, 2006; Schöftner, 2006; Schirrer, 2010). This work is based on the results of Schöftner (2006), Benatzky (2006), and Schirrer & Kozek (2008).

This text should provide the readers with first-hand experience of robust control design and implementation. It is intended to relate control theory results, simulation, and experimental results. This is done with the aim of improving one's understanding of relevant design parameters, caveats, and ways to successfully establish a working control law for challenging control problems. At the example of the application of modern control design methods to a complex, three-dimensional vibration control problem, a reliable methodology for tackling structurally new problems in vibration control is demonstrated. Additionally, the novel application of large-scale Piezo stack actuators for the vibration control of large and heavy flexible structures is studied.

This chapter is structured as follows: In the first section, a system description of the flexible metro car is given. The equations of motions are expressed by a first-order state-space representation obtained by a finite element analysis within the frequency range of interest. Details about the actuation, measurement, and performance variables are introduced which play an essential role for the MIMO controller design. Since the system order of the optimal state-space controller is equal to the order of the open-loop system, system order reduction is often necessary. The control laws designed for low-order plants then have to be validated on the original system for closed-loop stability and performance. Two types of optimal controllers are designed for a reduced-order plant model: an LQG and a weighted $\mathcal{H}_2$ controller. Simulation results are analysed and interpreted.

In an additional section, real-time control laws are designed with both design methodologies for a laboratory scale model of a rail car body. The redesigned controllers are validated in experimental test runs, providing an extended understanding on robustness, design parameter tuning, and real-time implementation issues. Finally, conclusions are drawn from both theoretical and experimental experience, and specific properties of the design methods are discussed.

2. System description - modeling of a flexible rail car body

2.1 Flexible rail car body model

For the different controller design procedures which will be explained in the next chapters a mathematical model of the flexible rail car body is necessary. The equations of motion of a linear time-invariant system can be stated in state-space form as:

$$\begin{aligned} \dot{\boldsymbol{x}} &= \boldsymbol{A}\boldsymbol{x} + \boldsymbol{B}_1\boldsymbol{w} + \boldsymbol{B}_2\boldsymbol{u} \\ \boldsymbol{z} &= \boldsymbol{C}_1\boldsymbol{x} + \boldsymbol{D}_{11}\boldsymbol{w} + \boldsymbol{D}_{12}\boldsymbol{u} \\ \boldsymbol{y} &= \boldsymbol{C}_2\boldsymbol{x} + \boldsymbol{D}_{21}\boldsymbol{w} + \boldsymbol{D}_{22}\boldsymbol{u}, \end{aligned} \tag{1}$$

where the first line describes the differential equation of the physical system. The second and third lines are the output equations. The system matrix of the dynamic system and the input

matrices for the disturbance $\boldsymbol{w}$ and the actuation $\boldsymbol{u}$ are denoted by $\boldsymbol{A}$, $\boldsymbol{B}_1$, and $\boldsymbol{B}_2$, respectively. The output matrices $\boldsymbol{C}_1$ and $\boldsymbol{C}_2$ as well as the feedthrough matrices $\boldsymbol{D}_{11}$, $\boldsymbol{D}_{12}$, $\boldsymbol{D}_{21}$, and $\boldsymbol{D}_{22}$ depend on the locations and on the types of the measurements and the performance outputs. In the literature on $\mathcal{H}_2$ and $\mathcal{H}_\infty$ controller design, $\boldsymbol{z}$ is called the output performance vector to be optimized and $\boldsymbol{y}$ is the measurement vector.

The state-space model description (1) can be established through analytical modeling, typically via the Finite Element (FE) Method, or through data-based identification. These steps are detailed in Kozek et al. (2011) for the rail car body model. In this work, the simulation part is based on an analytic model and the experimental part utilizes a model identified from measured signal data.

Fig. 1 shows the rail car body containing the positions for the performance outputs ($P_1 - P_6$), the disturbances ($E_1 - E_4$), the feedback sensors ($S_1 - S_4$), and the actuators ($A_1 - A_4$). For a detailed discussion on optimal placement of sensors and actuators see Schirrer (2010).

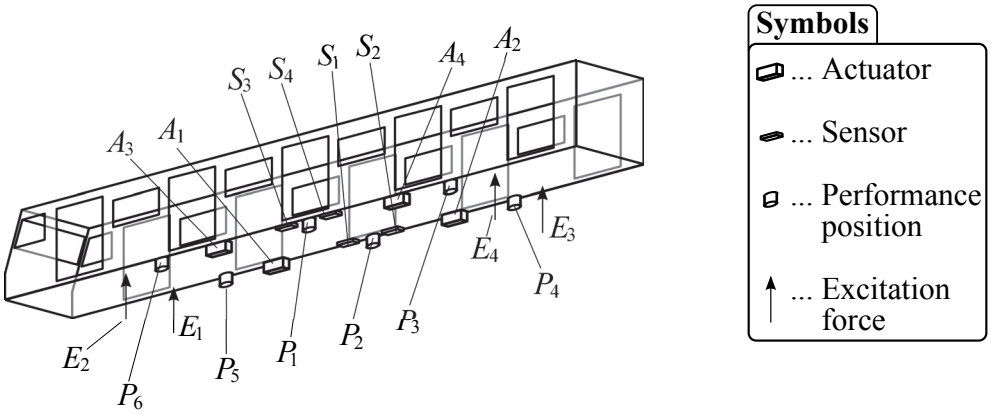

Fig. 1. Flexible rail car body: positions of input and output variables

The mathematical model of the rail car body, obtained by an FE model and subsequent order reduction steps, considers 17 elastic modes and 12 frequency-response-modes (FRM), see Schandl (2005). It is thus of order 58.

Fig. 2 shows the minimum and maximum singular values of the open-loop transfer function matrix $\boldsymbol{T}_{dz}$ which may be interpreted as the best- and the worst-case functional relationship from the white-noise disturbance vector $\boldsymbol{d}$ (related to $\boldsymbol{w}$ as shown below in Sec. 2.2) to the performance vector $\boldsymbol{z}$. From the singular values of the frequency response (which is identical to the Bode magnitude response in the SISO case), one can observe the elastic modes in the frequency range $\omega = 40 - 200\,\mathrm{rad/s}$ (region 2, blue circles) as well as the FRM in the higher frequency domain (region 3, red squares). Note that no suspension (rigid-body) modes are modeled that typically lie at low frequencies (region 1), because only the flexible car body structure is considered. Full multi-body validation is studied via extensive co-simulations in Schirrer (2010). The main goal in the next sections is to design controllers which suppress elastic modes, but which are not active at other frequencies because the accuracy of the simulation model decreases with increasing frequency. The transfer function is likely to be dominated by other physical effects and nonlinearities for $\omega > 200\,\mathrm{rad/s}$ which have not been considered in obtaining the mathematical model. The FRM are special modes, which

are necessary to accurately describe highly localized deformations caused by the structure actuation at the actuator interfaces (see Schandl (2005)). They lie at high frequencies and can be treated here as testing modes, since the actuator action in the high-frequency domain is undesired. High-frequency modes that are always present in continuous structures, but which are not considered in the model used for the controller design may be excited and destabilize the closed-loop system.

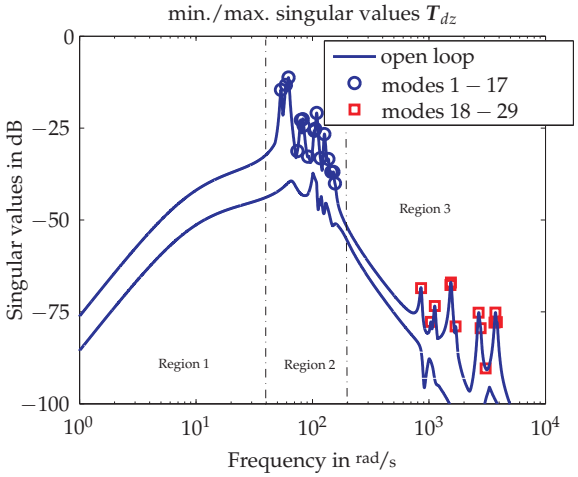

Fig. 2. Minimum and maximum singular values of the open-loop system showing the elastic modes. Modes denoted by squares are the frequency response modes (see Sec. 2.1).

2.2 Excitation

The rail vehicle runs on an imperfect track with misalignments and rail position variations. This track excitation is often characterized by its spatial frequency spectrum and associated filters, see Frederich (1984). For the studied rail car body dynamics, the disturbance $\boldsymbol{w}$ models the excitation of the car body by secondary suspension forces. Its spectrum is known from simulation and measurements and can be modeled by a colored noise sequence resulting from filtering a white noise disturbance input signal $\boldsymbol{d}$ by a second-order lag function with cut-off frequency $\omega_{\text{c.o.}} = 10\,\text{rad/s}$:

$$F(s) = 3000\frac{100}{s^2 + 20s + 100}. \tag{2}$$

The colored noise $\boldsymbol{w}(t)$ is related to the white noise signal $\boldsymbol{d}(t)$ by

$$\boldsymbol{W}(s) = F(s)\boldsymbol{D}(s) \quad \Leftrightarrow \quad \boldsymbol{w}(t) = \mathcal{L}^{-1}\{F(s)\boldsymbol{D}(s)\} \quad \text{with} \quad \boldsymbol{d}(t) = \mathcal{L}^{-1}\{\boldsymbol{D}(s)\}. \tag{3}$$

2.3 Actuators

A novel concept of structural actuation is applied here: Piezo stack actuators, mounted in consoles at the floor support trusses of the car body structure locally introduce bending moments into the structure. This allows direct actuation of the structural vibrations and is thus considered efficient. In this study, four stack actuators are considered in the full-size car body simulations (see Section 3 and Figure 1), whereas two stack actuators are utilized

in the experimental setup in Section 3.4, see Figure 25. For more detailed studies on the actuator concept refer to Kozek et al. (2011); the deformation characteristics of a simple console interface structure with a large-scale Piezo stack actuator have been investigated in Schirrer et al. (2008).

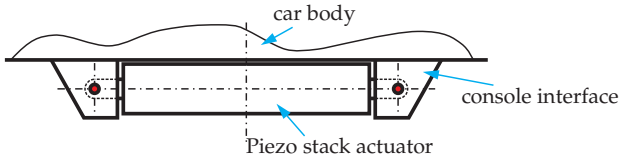

Fig. 3. Actuator mounted in a console to introduce torques into the attached flexible structure (rail car body)

2.4 Measurements

For the controller design, a signal-to-noise ratio (SNR) of about 10 is assumed, see Fig. 4. Two types of measurements are available: either using the acceleration or using strain sensor outputs proportional to the local structure curvature. The measurement positions are either collocated with the actuator or located in the middle of the car body underneath the doors (see Fig. 1). The latter case, when the actuator and sensor positions do not coincide, is called non-collocation. In general, non-collocated systems suffer from a lack of robustness and should not be used if the uncertainty of the system is large, but the controller performance may be better than for collocated systems if a sufficiently accurate mathematical model is available, see Preumont (2006).

In the present work, four strain sensors respectively six acceleration sensors are utilized in the full-size car body simulations. In the experimental setup, two strain sensors respectively one acceleration sensor are utilized for feedback (however, ride comfort performance is evaluated always at six acceleration performance positions as indicated in Figure 1).

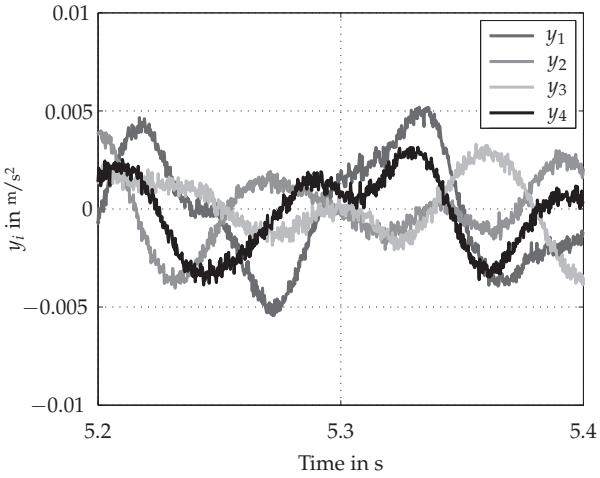

Fig. 4. Measured acceleration signals of the sensors showing a signal-to-noise ratio SNR = 10

2.5 Evaluation of passenger ride comfort according to ISO 2631

Whole-body vibrations are transmitted to the human body of the passengers in a bus, train or when driving a car. The ISO 2631 standard provides an average, empirically verified objective quantification of the level of perceived discomfort due to vibrations for human passengers (ISO, 1997). The accelerations in vertical and horizontal directions are filtered and these signals' root mean square (RMS) are combined into a scalar comfort quantity. Fig. 5 shows the ISO 2631 filter magnitude for vertical accelerations which are considered the only relevant component in the present study. For the heavy metro car, the highest sensitivity of a human occurs in the frequency range of $f \approx 4 - 10\,\mathrm{Hz}$. For the scaled laboratory model, all relevant eigenfrequencies are shifted by a factor of 8 compared to the full-size FEM model. For this reason, the ISO 2631 comfort filters and the excitation spectra are also shifted by this factor. Moreover, only unidirectional vertical acceleration signals are utilized as they represent the main contributions for the considered application.

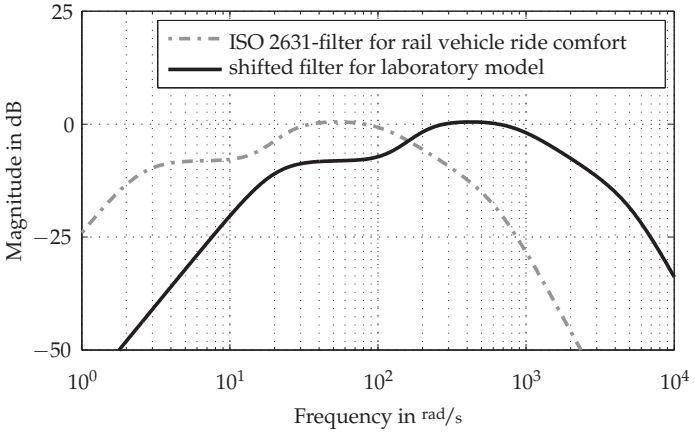

Fig. 5. Filter function according to ISO 2631 (yaw axis)

3. Optimal controller design for the metro car body

Two different methods for controller design are investigated in the following: an LQG and a frequency-weighted $\mathcal{H}_2$ controller are computed for a reduced-order plant model containing only the first 6 eigenmodes. The goal of this study is to obtain a deeper understanding on robustness and controller parameter tuning, since the LQG and the frequency-weighted $\mathcal{H}_2$ control methods are applied to design real-time state-space controllers for the laboratory setup in the next chapter.

3.1 LQG controller for a reduced-order system

3.1.1 Theory

The continuous-time linear-quadratic-gaussian (LQG) controller is a combination of an optimal linear-quadratic state feedback regulator (LQR) and a Kalman-Bucy state observer, see Skogestad & Postlethwaite (1996). Let a continuous-time linear-dynamic plant subject to

process and measurement noises be given in state space ($\boldsymbol{D} = \boldsymbol{0}$ for compactness):

$$\begin{aligned} \dot{\boldsymbol{x}} &= \boldsymbol{A}\boldsymbol{x} + \boldsymbol{B}\boldsymbol{u} + \boldsymbol{E}\boldsymbol{w} \\ \boldsymbol{y} &= \boldsymbol{C}\boldsymbol{x} + \boldsymbol{v}, \end{aligned} \tag{4}$$

where $\boldsymbol{w}$ and $\boldsymbol{v}$ are assumed to be uncorrelated zero-mean Gaussian stochastic (white-noise) processes with constant power spectral density matrices $\boldsymbol{W}$ and $\boldsymbol{V}$.
The LQG control law that minimizes the scalar integral-quadratic cost function

$$J = \mathrm{E}\left[\lim_{T\to\infty} \frac{1}{T} \int_0^T l(\boldsymbol{x}, \boldsymbol{u}) \mathrm{d}t\right] \tag{5}$$

with

$$l(\boldsymbol{x}, \boldsymbol{u}) = \boldsymbol{x}^{\mathrm{T}} \boldsymbol{Q} \boldsymbol{x} + \boldsymbol{u}^{\mathrm{T}} \boldsymbol{R} \boldsymbol{u} \tag{6}$$

turns out to be of the form

$$\dot{\hat{\boldsymbol{x}}} = \boldsymbol{A}\hat{\boldsymbol{x}} + \boldsymbol{B}\boldsymbol{u} + \boldsymbol{H}(\boldsymbol{y} - \boldsymbol{C}\hat{\boldsymbol{x}}) \tag{7}$$

$$\boldsymbol{u} = \qquad -\boldsymbol{K}_{\mathrm{LQR}}\hat{\boldsymbol{x}}. \tag{8}$$

Thereby, $\mathrm{E}[\cdot]$ is the expected value operator, $\boldsymbol{Q} = \boldsymbol{Q}^{\mathrm{T}} \succeq 0$ and $\boldsymbol{R} = \boldsymbol{R}^{\mathrm{T}} \succ 0$ are constant, positive (semi-)definite weighting matrices (design parameters) which affect the closed-loop properties, (7) is the Kalman observer equation, and (8) is the LQR state feedback control law utilizing the state estimate.
The optimal LQR state feedback control law (Skogestad & Postlethwaite, 1996)

$$\boldsymbol{u} = -\boldsymbol{K}_{\mathrm{LQR}}\boldsymbol{x} \tag{9}$$

minimizes the deterministic cost function

$$J = \int_0^\infty l(\boldsymbol{x}, \boldsymbol{u}) \mathrm{d}t \tag{10}$$

and is obtained by

$$\boldsymbol{K}_{\mathrm{LQR}} = \boldsymbol{R}^{-1}\boldsymbol{B}^{\mathrm{T}}\boldsymbol{X}, \tag{11}$$

where $\boldsymbol{X}$ is the unique positive-semidefinite solution of the algebraic Riccati equation

$$\boldsymbol{A}^{\mathrm{T}}\boldsymbol{X} + \boldsymbol{X}\boldsymbol{A} - \boldsymbol{X}\boldsymbol{B}\boldsymbol{R}^{-1}\boldsymbol{B}^{\mathrm{T}}\boldsymbol{X} + \boldsymbol{Q} = \boldsymbol{0}. \tag{12}$$

The unknown system states $\boldsymbol{x}$ can be estimated by a general state-space observer (Luenberger, 1964). The estimated states are denoted by $\hat{\boldsymbol{x}}$, and the state estimation error $\boldsymbol{\varepsilon}$ is defined by

$$\boldsymbol{\varepsilon} := \boldsymbol{x} - \hat{\boldsymbol{x}}. \tag{13}$$

Choosing the linear relation

$$\dot{\hat{\boldsymbol{x}}} = \boldsymbol{F}\hat{\boldsymbol{x}} + \boldsymbol{G}\boldsymbol{u} + \boldsymbol{H}\boldsymbol{y}, \tag{14}$$

for state estimation, the following error dynamics is obtained:

$$\dot{\boldsymbol{\varepsilon}} = \boldsymbol{F}\boldsymbol{\varepsilon} + (\boldsymbol{A} - \boldsymbol{H}\boldsymbol{C} - \boldsymbol{F})\boldsymbol{x} + (\boldsymbol{B} - \boldsymbol{G})\boldsymbol{u}. \tag{15}$$

If $\boldsymbol{F} = \boldsymbol{A} - \boldsymbol{HC}$ and $\boldsymbol{G} = \boldsymbol{B}$ hold, and if the real parts of the eigenvalues of $\boldsymbol{F}$ are negative, the error dynamics is stable, $\hat{\boldsymbol{x}}$ converges to the plant state vector $\boldsymbol{x}$, and the observer equation (7) is obtained.
With the given noise properties, the optimal observer is a Kalman-Bucy estimator that minimizes $\mathrm{E}\left[\boldsymbol{\varepsilon}^{\mathrm{T}}\boldsymbol{\varepsilon}\right]$ (see Mohinder & Angus (2001); Skogestad & Postlethwaite (1996)). The observer gain $\boldsymbol{H}$ in (7) is given by

$$\boldsymbol{H} = \boldsymbol{Y}\boldsymbol{C}^{\mathrm{T}}\boldsymbol{V}^{-1}, \tag{16}$$

where $\boldsymbol{Y}$ is the solution of the (filter) algebraic Riccati equation

$$\boldsymbol{A}\boldsymbol{Y} + \boldsymbol{Y}\boldsymbol{A}^{\mathrm{T}} - \boldsymbol{Y}\boldsymbol{C}^{\mathrm{T}}\boldsymbol{V}^{-1}\boldsymbol{C}\boldsymbol{Y} + \boldsymbol{E}\boldsymbol{W}\boldsymbol{E}^{\mathrm{T}} = \boldsymbol{0}. \tag{17}$$

Taking into account the separation principle (Skogestad & Postlethwaite, 1996), which states that the closed-loop system eigenvalues are given by the state-feedback regulator dynamics $\boldsymbol{A} - \boldsymbol{BK}$ together with those of the state-estimator dynamics $\boldsymbol{A} - \boldsymbol{HC}$, one finds the stabilized regulator-observer transfer function matrix

$$\boldsymbol{G_{yu}}(s) = -\boldsymbol{K}[s\mathbf{I} - \boldsymbol{A} + \boldsymbol{HC} + \boldsymbol{BK}]^{-1}\boldsymbol{H}\,. \tag{18}$$

Remark: The solutions to the algebraic Riccati equations (12) and (17) and thus the LQG controller exist if the state-space systems $\left(\boldsymbol{A}, \boldsymbol{B}, \boldsymbol{Q}^{\frac{1}{2}}\right)$ and $\left(\boldsymbol{A}, \boldsymbol{W}^{\frac{1}{2}}, \boldsymbol{C}\right)$ are stabilizable and detectable (see Skogestad & Postlethwaite (1996)).

3.1.2 LQG controller design and results for strain sensors / non-collocation

The controller designs are based on a reduced-order plant model which considers only the lowest 6 eigenmodes. The smallest and largest singular values of the system are shown in Fig. 6 and Fig. 7 (compare Fig. 2 for the complete system). The eigenvalues are marked by blue circles. The red lines depict the singular values of the order-reduced $\boldsymbol{T}_{dz,\mathrm{red}}$ (including the shaping filter (2) for the colored noise of the disturbance signal $\boldsymbol{w}$).
Since a reduced-order system is considered for the controller design, the separation principle is not valid any longer for the full closed-loop system. Neither the regulator gain $\boldsymbol{K}_{\mathrm{LQR}}$ nor the estimator gain $\boldsymbol{H}$ is allowed to become too large, otherwise spillover phenomena may occur that potentially destabilize the high-frequency modes. Therefore, the design procedure is an (iterative) trial-and-error loop as follows: in a first step, the weighting matrices for the regulator are prescribed and the resulting regulator gain is used for the full-order system where it is assumed that the state vector can be completely measured. If spillover occurs, the controller action must be reduced by decreasing the state weighting $\boldsymbol{Q}$. In a second step, the design parameters for the Kalman-Bucy-filter are chosen, considering the fact that the process noise $\boldsymbol{w}$ is no white noise sequence any longer, see (2). Since the process noise covariance is approximately known as $(84.54\,\mathrm{N})^2$ for each channel, the weighting for the output noise $\boldsymbol{V}$ is utilized as a design parameter.
For the optimal regulator the weighting matrices for the states and the input variables are chosen as

$$\boldsymbol{Q} = 9 \cdot 10^8 \cdot \mathbf{I}_{12\times 12}, \qquad \boldsymbol{R} = \mathbf{I}_{4\times 4}, \tag{19}$$

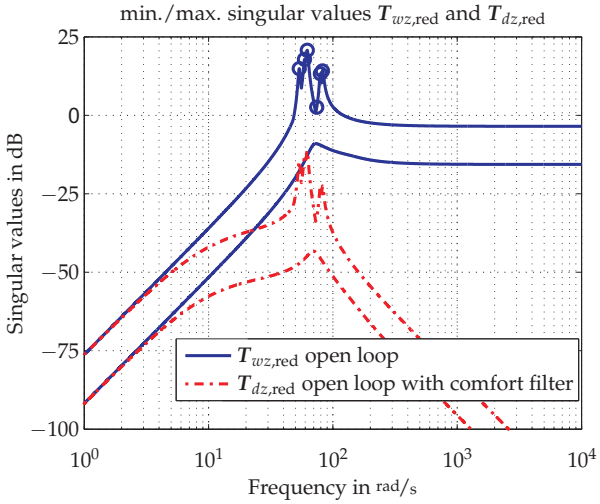

Fig. 6. Smallest and largest singular values of the reduced-order open-loop system (6 modes)

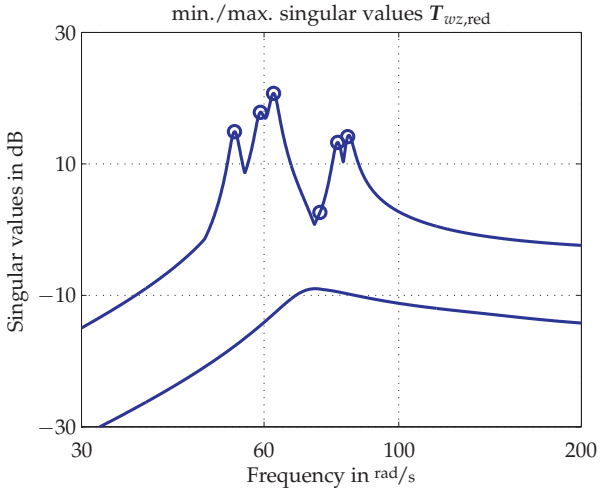

Fig. 7. Smallest and largest singular values of the reduced-order open-loop system (6 modes, zoomed)

where $\mathbf{I}_{n\times n}$ is the identity matrix (n rows, n columns). The observer weightings are chosen to be

$$\boldsymbol{W} = 84.54^2 \cdot \mathbf{I}_{4\times 4}, \qquad \boldsymbol{V} = (1.54 \cdot 10^{-6})^2 \cdot \mathbf{I}_{4\times 4}. \tag{20}$$

Table 1 lists the reduction of the ISO-filtered (see Fig. 5) RMS of each performance variable $z_{1,\mathrm{ISO}}$–$z_{6,\mathrm{ISO}}$ compared to open-loop results. Figures 8–11 contain the maximum/minimum singular values from the white noise input $\boldsymbol{d}$ (which is related to the colored noise input $\boldsymbol{w}$ by (3)) to the performance vector $\boldsymbol{z}$, the time-domain response of two selected performance

variables z_1 and z_6, and two pole location plots (overview and zoomed) for the open- and the closed-loop results.

Performance position index i	1	2	3	4	5	6	avg.
RMS reduction $z_{i,\mathrm{ISO}}$ in %	8.44	11.22	29.64	26.53	30.05	31.80	22.94

Table 1. RMS reduction of the performance vector $\boldsymbol{z}$ by LQG control (strain sensors / non-collocation), system order 12

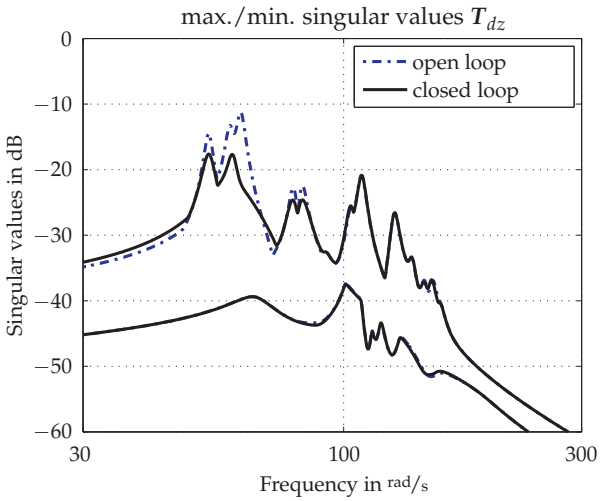

Fig. 8. Reduction of rail car disturbance transfer singular values with non-collocated LQG control

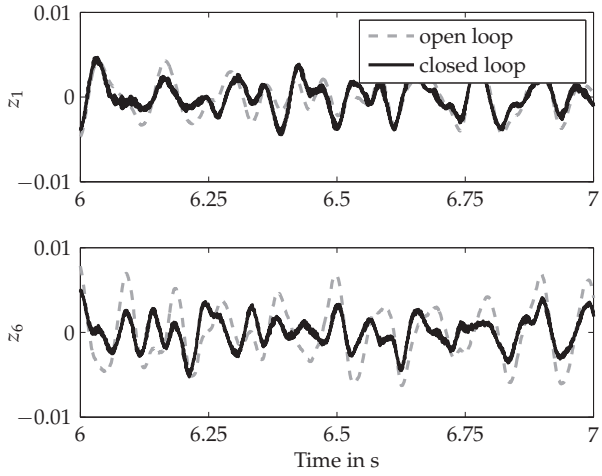

Fig. 9. Acceleration signals z_1 and z_6 without/with non-collocated LQG control

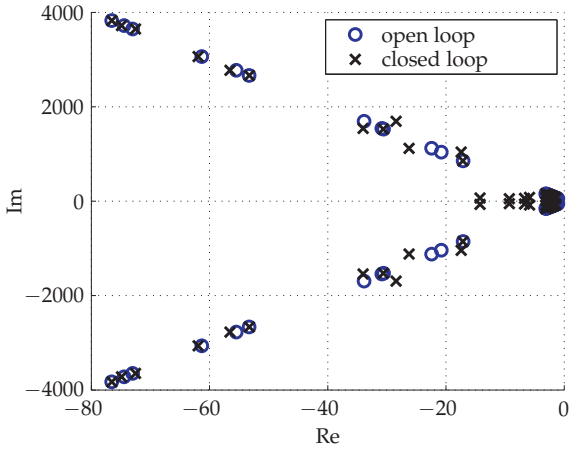

Fig. 10. Rail car model open-loop and non-collocated LQG closed-loop pole locations

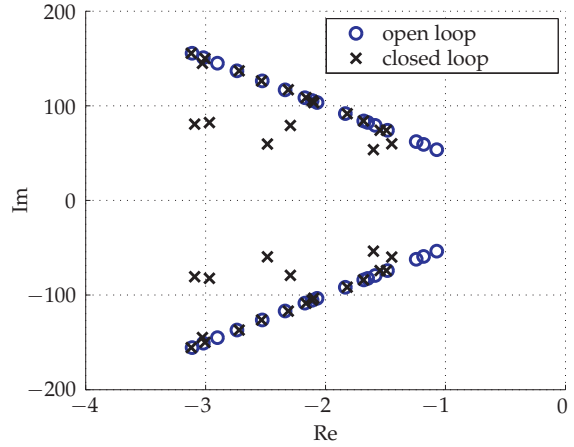

Fig. 11. Rail car model open-loop and non-collocated LQG closed-loop pole locations (zoomed)

3.1.3 Controller design and results for acceleration sensors / collocation

The optimal regulator is designed with the same weighting matrices for the states and the control variables as for the case strain sensors / non-collocation, see (19). The observer weightings are chosen to be

$$\boldsymbol{W} = 84.54^2 \cdot \mathbf{I}_{4\times 4}, \qquad \boldsymbol{V} = 0.154^2 \cdot \mathbf{I}_{4\times 4}. \tag{21}$$

Table 2 lists the reduction of the ISO-filtered (see Fig. 5) RMS of each performance variable $z_{1,\mathrm{ISO}}$–$z_{6,\mathrm{ISO}}$ compared to open-loop results. Figures 12–15 contain the maximum/minimum singular values from the white noise input $\boldsymbol{d}$ (which is related to the colored noise input $\boldsymbol{w}$

by (3)) to the performance vector z, the time-domain response of two selected performance variables z_1 and z_6, and two pole location plots (overview and zoomed) for the open- and the closed-loop results.

Performance position index i	1	2	3	4	5	6	avg.
RMS reduction $z_{i,\mathrm{ISO}}$ in %	7.83	8.36	8.04	7.02	8.79	10.23	8.38

Table 2. RMS reduction of the performance vector z by LQG control (acceleration sensors / collocation), system order 12

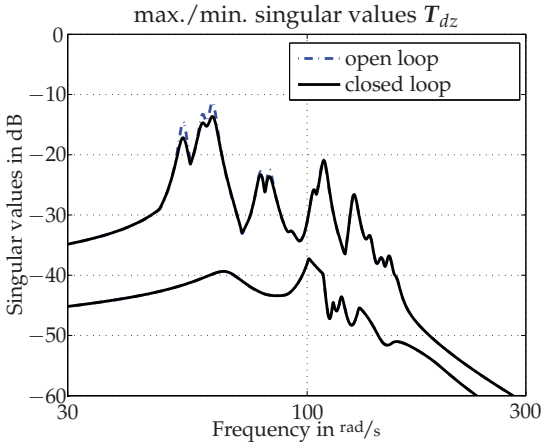

Fig. 12. Reduction of rail car disturbance transfer singular values with collocated LQG control

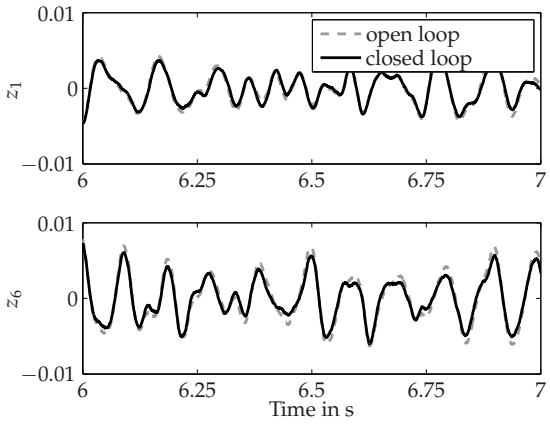

Fig. 13. Acceleration signals z_1 and z_6 without/with collocated LQG control

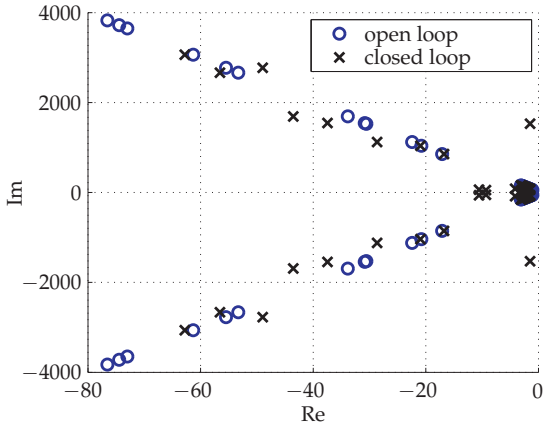

Fig. 14. Rail car model open-loop and collocated LQG closed-loop pole locations

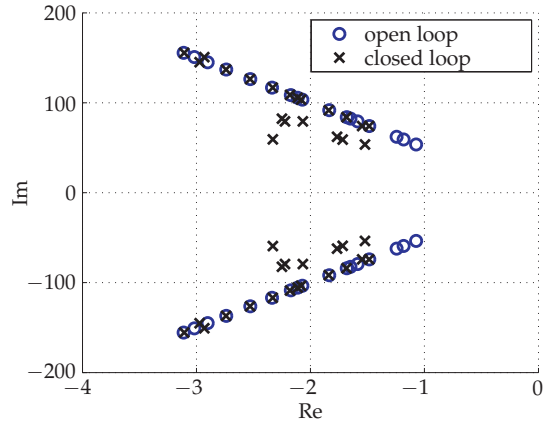

Fig. 15. Rail car model open-loop and collocated LQG closed-loop pole locations (zoomed)

3.2 Frequency-weighted $\mathcal{H}_2$ controller for a reduced-order system

The LQG controllers designed in the previous section do not take into account the performance vector z. The design of the regulator and the estimator gains are a trade-off between highly-damped modes, expressed by the negative real part of the closed-loop poles, and robustness considerations. The generalization of the LQG controller is the $\mathcal{H}_2$ controller, which explicitly considers the performance vector (e.g. one can minimize the deflection 2-norm at a certain point of a flexible system). Another advantage of this type of optimal controller is the possibility to utilize frequency-domain weighting functions. In doing so, the controller action can be shaped for specific target frequency ranges. In turn, the controller can be designed not to influence the dynamic behaviour where the mathematical model is uncertain or sensitive to parameter variations.

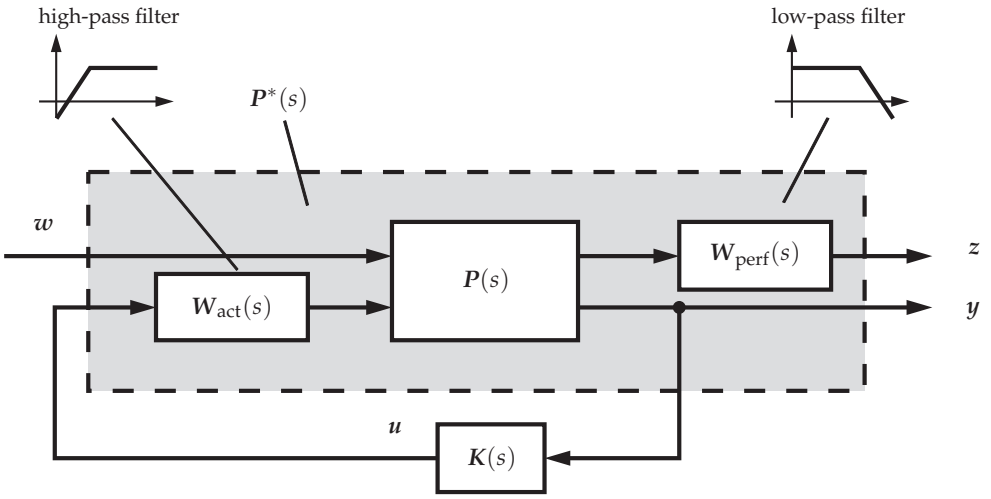

Fig. 16. Closed-loop system $\boldsymbol{P}(s)$ with controller $\boldsymbol{K}(s)$ and actuator and performance weighting functions $\boldsymbol{W}_{\text{act}}(s)$ and $\boldsymbol{W}_{\text{perf}}(s)$

Fig. 16 shows the closed-loop system, where the system dynamics, the controller, and the frequency-weighted transfer functions are denoted by $\boldsymbol{P}(s)$, $\boldsymbol{K}(s)$, $\boldsymbol{W}_{\text{act}}(s)$, and $\boldsymbol{W}_{\text{perf}}(s)$. Taking into account the frequency-weights in the system dynamics, the weighted system description of $\boldsymbol{P}^*$ can be formulated:

$$\begin{bmatrix} \boldsymbol{z} \\ \boldsymbol{y} \end{bmatrix} = \begin{bmatrix} \boldsymbol{P}_{11}^*(s) & \boldsymbol{P}_{12}^*(s) \\ \boldsymbol{P}_{21}^*(s) & \boldsymbol{P}_{22}^*(s) \end{bmatrix} \begin{bmatrix} \boldsymbol{w} \\ \boldsymbol{u} \end{bmatrix}, \tag{22}$$

where $\boldsymbol{P}_{11}^*(s)$, $\boldsymbol{P}_{12}^*(s)$, $\boldsymbol{P}_{21}^*(s)$, and $\boldsymbol{P}_{22}^*(s)$ are the Laplace domain transfer functions from the input variables $\boldsymbol{u}$ and $\boldsymbol{w}$ to the output variables $\boldsymbol{y}$ and $\boldsymbol{z}$.

3.2.1 $\mathcal{H}_2$ control theory

Let the system dynamics be given in the state-space form (1), fulfilling the following prerequisites (see Skogestad & Postlethwaite (1996)):

- $(\boldsymbol{A}, \boldsymbol{B}_2)$ is stabilizable
- $(\boldsymbol{C}_2, \boldsymbol{A})$ is detectable
- $\boldsymbol{D}_{11} = \boldsymbol{0}, \boldsymbol{D}_{22} = \boldsymbol{0}$
- $\boldsymbol{D}_{12}$ has full rank
- $\boldsymbol{D}_{21}$ has full rank
- $\begin{bmatrix} \boldsymbol{A} - \mathrm{j}\omega\mathbf{I} & \boldsymbol{B}_2 \\ \boldsymbol{C}_1 & \boldsymbol{D}_{12} \end{bmatrix}$ has full column rank for all ω

- $\begin{bmatrix} \boldsymbol{A} - \mathrm{j}\omega\mathbf{I} & \boldsymbol{B}_1 \\ \boldsymbol{C}_2 & \boldsymbol{D}_{21} \end{bmatrix}$ has full row rank for all ω

For compactness the following abbreviations are introduced:

$$\begin{aligned}
\overline{\boldsymbol{R}} &= \boldsymbol{D}_{12}{}^{\mathrm{T}}\boldsymbol{D}_{12} \\
\overline{\boldsymbol{S}} &= \boldsymbol{B}_2\overline{\boldsymbol{R}}^{-1}\boldsymbol{B}_2{}^{\mathrm{T}} \\
\overline{\boldsymbol{A}} &= \boldsymbol{A} - \boldsymbol{B}_2\overline{\boldsymbol{R}}^{-1}\boldsymbol{D}_{12}{}^{\mathrm{T}}\boldsymbol{C}_1 \\
\overline{\boldsymbol{Q}} &= \boldsymbol{C}_1{}^{\mathrm{T}}\boldsymbol{C}_1 - \boldsymbol{C}_1{}^{\mathrm{T}}\boldsymbol{D}_{12}\overline{\boldsymbol{R}}^{-1}\boldsymbol{D}_{12}{}^{\mathrm{T}}\boldsymbol{C}_1 \succeq \mathbf{0} \\
\overline{\overline{\boldsymbol{R}}} &= \boldsymbol{D}_{21}\boldsymbol{D}_{21}{}^{\mathrm{T}} \\
\overline{\overline{\boldsymbol{S}}} &= \boldsymbol{C}_2{}^{\mathrm{T}}\overline{\overline{\boldsymbol{R}}}^{-1}\boldsymbol{C}_2 \\
\overline{\overline{\boldsymbol{A}}} &= \boldsymbol{A} - \boldsymbol{B}_1\boldsymbol{D}_{21}{}^{\mathrm{T}}\overline{\overline{\boldsymbol{R}}}^{-1}\boldsymbol{C}_2 \\
\overline{\overline{\boldsymbol{Q}}} &= \boldsymbol{B}_1\boldsymbol{B}_1{}^{\mathrm{T}} - \boldsymbol{B}_1\boldsymbol{D}_{21}{}^{\mathrm{T}}\overline{\overline{\boldsymbol{R}}}^{-1}\boldsymbol{D}_{21}\boldsymbol{B}_1{}^{\mathrm{T}} \succeq \mathbf{0},
\end{aligned}$$

where $\succeq \mathbf{0}$ denotes positive-semidefiniteness of the left-hand side. The $\mathcal{H}_2$ control design generates the controller transfer function $\boldsymbol{K}(s)$ which minimizes the $\mathcal{H}_2$ norm of the transfer function $\boldsymbol{T}_{wz}$, or equivalently

$$\|\boldsymbol{T}_{wz}\|_2 = \sqrt{\frac{1}{2\pi}\int_{-\infty}^{\infty} \boldsymbol{T}_{wz}{}^{\mathrm{T}}(\mathrm{j}\omega)\boldsymbol{T}_{wz}(\mathrm{j}\omega)\mathrm{d}\omega} \to \min. \tag{23}$$

The controller gain $\boldsymbol{K}_c$ and the estimator gain $\boldsymbol{K}_f$ are determined by

$$\boldsymbol{K}_c = \overline{\boldsymbol{R}}^{-1}(\boldsymbol{B}_2{}^{\mathrm{T}}\boldsymbol{X}_2 + \boldsymbol{D}_{12}{}^{\mathrm{T}}\boldsymbol{C}_1) \tag{24}$$

and

$$\boldsymbol{K}_f = (\boldsymbol{Y}_2\boldsymbol{C}_2{}^{\mathrm{T}} + \boldsymbol{B}_1\boldsymbol{D}_{21}{}^{\mathrm{T}})\overline{\overline{\boldsymbol{R}}}^{-1}, \tag{25}$$

where $\boldsymbol{X}_2 \succeq \mathbf{0}$ and $\boldsymbol{Y}_2 \succeq \mathbf{0}$ are the solutions of the two algebraic Riccati equations

$$\boldsymbol{X}_2\overline{\boldsymbol{A}} + \overline{\boldsymbol{A}}^{\mathrm{T}}\boldsymbol{X}_2 - \boldsymbol{X}_2\overline{\boldsymbol{S}}\boldsymbol{X}_2 + \overline{\boldsymbol{Q}} = \mathbf{0}, \tag{26}$$

$$\overline{\overline{\boldsymbol{A}}}\boldsymbol{Y}_2 + \boldsymbol{Y}_2\overline{\overline{\boldsymbol{A}}}^{\mathrm{T}} - \boldsymbol{Y}_2\overline{\overline{\boldsymbol{S}}}\boldsymbol{Y}_2 + \overline{\overline{\boldsymbol{Q}}} = \mathbf{0}. \tag{27}$$

The state-space representation of the controller dynamics is given by

$$\begin{aligned}
\dot{\hat{\boldsymbol{x}}} &= (\boldsymbol{A} - \boldsymbol{B}_2\boldsymbol{K}_c - \boldsymbol{K}_f(\boldsymbol{C}_2 - \boldsymbol{D}_{22}\boldsymbol{K}_c))\hat{\boldsymbol{x}} + \boldsymbol{K}_f\boldsymbol{y} \\
\boldsymbol{u} &= -\boldsymbol{K}_c\hat{\boldsymbol{x}},
\end{aligned} \qquad \Rightarrow \boldsymbol{u} = -\boldsymbol{K}(s)\boldsymbol{y}. \tag{28}$$

3.2.2 $\mathcal{H}_2$ controller design and results for strain sensors / non-collocation

The frequency-weighting functions have been specified as

$$\boldsymbol{W}_{\mathrm{act}} = G_{\mathrm{act}} \cdot \mathbf{I}_{4\times 4} = 4967 \cdot \frac{(s+45)^4 \cdot (s^2 + 6s + 3034)}{(s+620)^4 \cdot (s+2000)^2} \cdot \mathbf{I}_{4\times 4} \tag{29}$$

$$\boldsymbol{W}_{\text{perf}} = G_{\text{perf}} \cdot \mathbf{I}_{6\times 6} = 20 \cdot \mathbf{I}_{6\times 6} \tag{30}$$

As in the previous section, the $\mathcal{H}_2$ controller is designed for the reduced-order model (12 states). Considering the shaping filter (2) for the disturbance ($8 = 4 \cdot 2$ states) and the weighting functions (29) and (30) ($24 = 4 \cdot 6$ states), one finds a controller of order 44.
Table 3 lists the reduction of the ISO-filtered (see Fig. 5) RMS of each performance variable $z_{1,\text{ISO}}$–$z_{6,\text{ISO}}$ compared to open-loop results. Figures 17–20 contain the maximum/minimum singular values from the white noise input $\boldsymbol{d}$ (which is related to the colored noise input $\boldsymbol{w}$ by (3)) to the performance vector $\boldsymbol{z}$, the time-domain response of two selected performance variables z_1 and z_6, and two pole location plots (overview and zoomed) for the open- and the closed-loop results.

Performance position index i	1	2	3	4	5	6	avg.
RMS reduction $z_{i,\text{ISO}}$ in %	26.27	27.95	28.71	27.84	30.99	34.31	29.35

Table 3. RMS reduction of the performance vector $\boldsymbol{z}$ by $\mathcal{H}_2$ control (strain sensors / non-collocation), system order 44

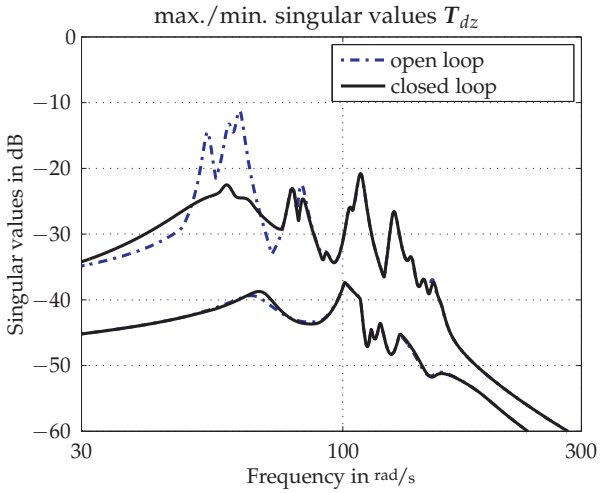

Fig. 17. Reduction of rail car disturbance transfer singular values with non-collocated $\mathcal{H}_2$ control

3.2.3 $\mathcal{H}_2$ controller design and results for acceleration sensors / collocation

The frequency-weighting functions have been specified as

$$\boldsymbol{W}_{\text{act}} = G_{\text{act}} \cdot \mathbf{I}_{4\times 4} = 4967 \cdot \frac{(s+45)^4 \cdot (s^2+6s+3034)}{(s+620)^4 \cdot (s+2000)^2} \cdot \mathbf{I}_{4\times 4}, \tag{31}$$

$$\boldsymbol{W}_{\text{perf}} = G_{\text{perf}} \cdot \mathbf{I}_{6\times 6} = 20 \cdot \mathbf{I}_{6\times 6}. \tag{32}$$

Table 4 lists the reduction of the ISO-filtered (see Fig. 5) RMS of each performance variable $z_{1,\text{ISO}}$–$z_{6,\text{ISO}}$ compared to open-loop results. Figures 21–24 contain the maximum/minimum singular values from the white noise input $\boldsymbol{d}$ (which is related to the colored noise input $\boldsymbol{w}$

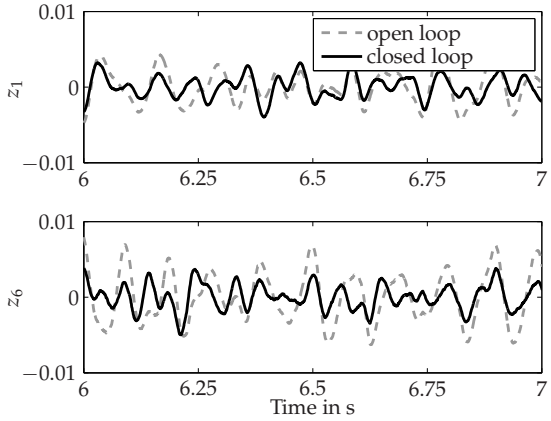

Fig. 18. Acceleration signals z_1 and z_6 without/with non-collocated $\mathcal{H}_2$ control

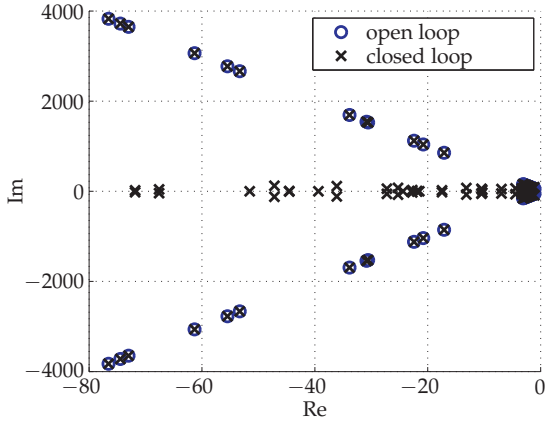

Fig. 19. Rail car model open-loop and non-collocated $\mathcal{H}_2$ closed-loop pole locations

by (3)) to the performance vector z, the time-domain response of two selected performance variables z_1 and z_6, and two pole location plots (overview and zoomed) for the open- and the closed-loop results.

Performance position index i	1	2	3	4	5	6	avg.
RMS reduction $z_{i,\mathrm{ISO}}$ in %	23.89	28.12	27.23	24.67	28.85	31.27	27.34

Table 4. RMS reduction of the performance vector z by $\mathcal{H}_2$ control (acceleration sensors / collocation), system order 44

3.3 Interpretation

The main goal for both the LQG and the $\mathcal{H}_2$ controller designs was to increase the damping of the first three eigenmodes. In the present design task, the LQG controller designed for

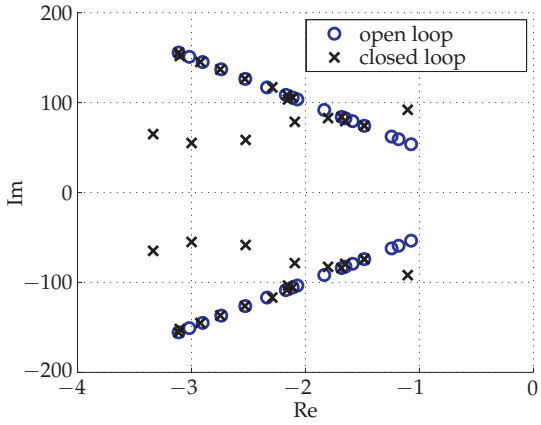

Fig. 20. Rail car model open-loop and non-collocated $\mathcal{H}_2$ closed-loop pole locations (zoomed)

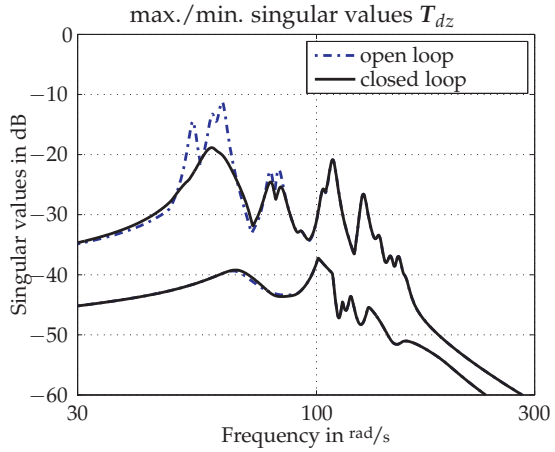

Fig. 21. Reduction of rail car disturbance transfer singular values with collocated $\mathcal{H}_2$ control

collocated acceleration sensors (see Section 3.1.3) did not yield satisfactory performance. The singular value plot shows only marginal magnitude reduction (Figure 12), and also a time-domain analysis of the performance signals z_1 and z_6 (see Figure 13) shows no significant improvement. According to Table 2, the reduction of the filtered performance vector is approximately 8%. However, at $\omega \approx 1500\,\mathrm{rad/s}$ one of the frequency response modes approaches the imaginary axis (Fig. 14 and Fig. 15). Even though the simulated closed loop remains stable, this spillover is critical for operation at an uncertain real plant which possesses unknown high-frequency dynamics.

Considering the LQG design for non-collocated strain sensors in Section 3.1.2, the controller significantly improves the vibrational behaviour. The performance vector is reduced by 23% (Table 1) and a significant reduction is apparent for the time-domain evaluation in Fig. 9. The maximum singular values of the first three eigenmodes are reduced (e.g. third eigenmode

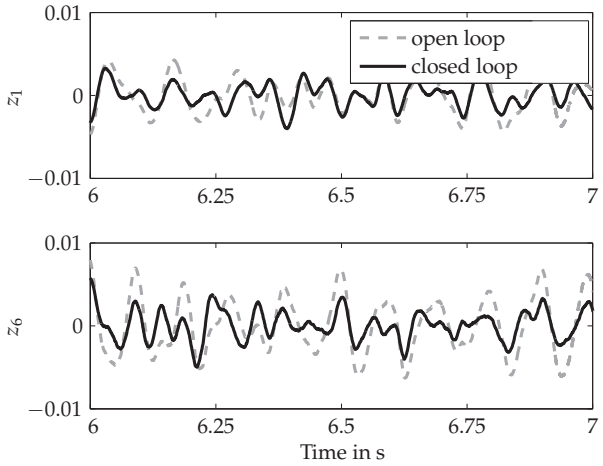

Fig. 22. Acceleration signals z_1 and z_6 without/with collocated $\mathcal{H}_2$ control

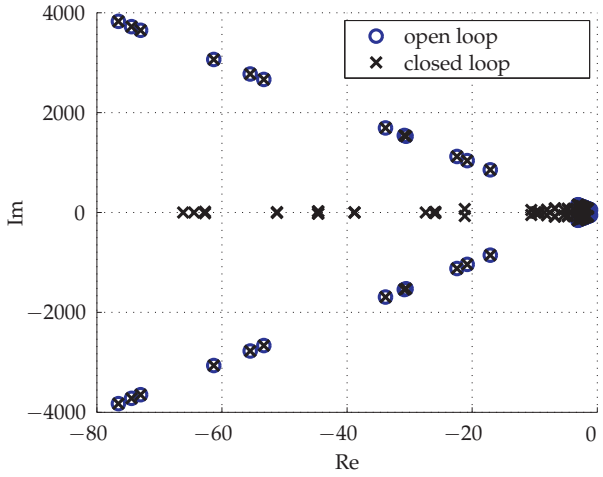

Fig. 23. Rail car model open-loop and collocated $\mathcal{H}_2$ closed-loop pole locations

−11 dB, see Fig. 8). From the pole location plot one concludes that in the higher frequency domain the frequency response modes remain unchanged (Fig. 10 and Fig. 11).
Both variants of the $\mathcal{H}_2$-optimal controllers (Section 3.2.2 and Section 3.2.3) show significantly higher performance in simulation than the controllers obtained by the LQG design procedure. The main advantage of the $\mathcal{H}_2$ design approach is the possibility to directly incorporate frequency weights to shape the design, see (29) and (31). Specifically, the frequency content of the actuator command signals can be modified. The control law actuates mainly within the frequency range $\omega \approx 50 - 70\,\mathrm{rad/s}$ due to the transmission zeros in the weighting functions $\boldsymbol{W}_{\mathrm{act}}$. In the high-frequency domain, $\boldsymbol{W}_{\mathrm{act}}$ is large for both $\mathcal{H}_2$ designs, so only small actuator signal magnitudes result at these frequencies which is especially

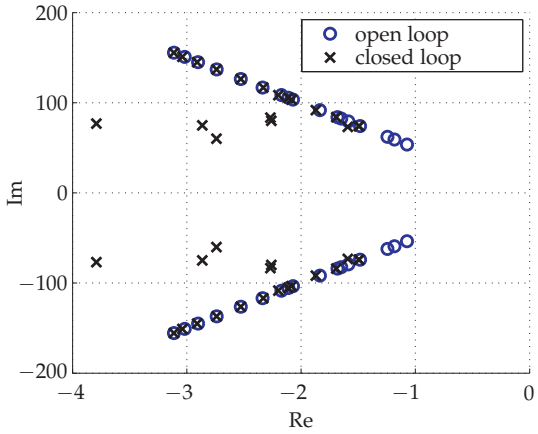

Fig. 24. Rail car model open-loop and collocated $\mathcal{H}_2$ closed-loop pole locations (zoomed)

favorable if the plant dynamics is unknown there. The results for strain/non-collocation and acceleration/collocation control designs are shown in Figs. 17–20 and Table 3 as well as in Figs. 21–24 and Table 4. In the first case the vibrations of the time-domain performance signals $z_{i,\mathrm{ISO}}$ are reduced by 30% (Fig. 18), which is also indicated by the singular values plot (Fig. 17): the lowest three modes are reduced on average by 11 dB. Virtually no spillover occurs at high frequencies ($\omega \approx 150 - 4000\,\mathrm{rad/s}$): The singular values are unchanged (not shown) and also the pole locations remain unchanged for $\omega > 150\,\mathrm{rad/s}$ (seen in Fig. 19 and Fig. 20 where the open-loop poles (blue circles) and closed-loop poles (black crosses) coincide).
The acceleration sensor / collocation simulation results show similar improvement: Only the first three modes are strongly damped (Fig. 21 and Fig. 24), the other ones are hardly affected by the controller action due to the specific choice of the weighting function (31), see Fig. 23. The average reduction of the ISO-filtered performance variables is 27% (Table 4 and Fig. 22).
As a concluding remark, note that the combination of the $\mathcal{H}_2$ method with frequency-weighted transfer functions for the input and the performance signals ($\boldsymbol{W}_{\mathrm{act}}$, $\boldsymbol{W}_{\mathrm{perf}}$) provide satisfactory results, which are characterized by their high robustness and insensitivity to parameter uncertainties. It is shown that the frequency content of the controller action can be tuned by the input weight $\boldsymbol{W}_{\mathrm{act}}$, which affects only the first modes of interest. Higher modes, which are much more difficult to model, are hardly affected due to the roll-off of the $\mathcal{H}_2$ controller. Nevertheless, the LQG controller shows very promising results for the case of non-collocated strain sensors, although the controller is designed for a strongly reduced model containing only 6 modes (note that the full order model has 29 modes). If the acceleration signals are measured and sensor and actuators are collocated, the full-order plant is destabilized by the LQG controller (designed on the reduced-order plant).
Finally, it is noted that so-called reduced-order LQG controllers (see Gawronski (2004)) also have been designed to control the metro vehicle, see Schöftner (2006). By this method an LQG controller has been directly designed for the full-order plant model with 29 modes. Then, the controller transfer functions are evaluated (dynamic systems of order 58) and transformed to the Gramian-based input/output-balanced form. Hardly observable or controllable states, indicated by small Hankel singular values, are truncated, yielding a

low-order controller. While this procedure works well for academic problems (for example, a simply-supported beam), for the metro car body no low-order controller with good vibration reduction performance could be found, see Schöftner (2006).

3.4 Experimental setup of scaled metro car body

3.4.1 General remarks

Fig. 25 and Fig. 26 show the laboratory testbed in which the metro car body scale model is operated. The aluminum structure is excited via an electrodynamic shaker, two Piezo patches measure local structure strain, and two Piezo stack actuators, mounted in consoles on the structure, provide an efficient means of structural actuation. Fig. 26 also shows the actuation and measurement setup symbolically with actuator amplifier (AA), shaker amplifier (SA), antialiasing filters (AF), measurement amplifier (MA) and the laboratory computer (Lab.-PC) on which the real-time control algorithms are implemented.

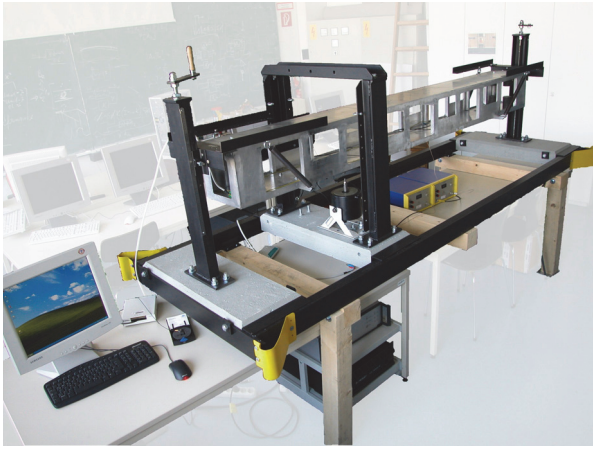

Fig. 25. Scaled metro car body

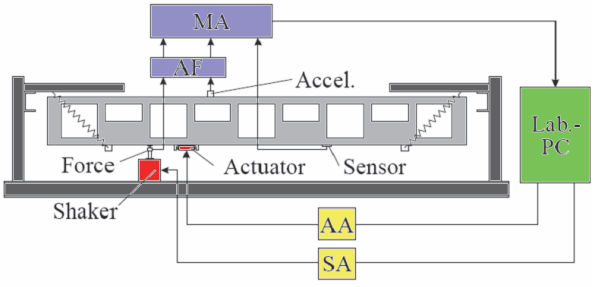

Fig. 26. Basic sketch of the scaled metro car body with actuators, sensors, and performance variables

The pole plot and the singular-value plot (Fig. 27 and Fig. 28) of the frequency response provide information on the identified dynamics of the laboratory setup (200 modes): the modes relevant for the control problem are the bending mode at $f \approx 65\,\text{Hz}$ and the torsional

mode at $f \approx 75\,\text{Hz}$. The majority of the poles are either negligible high-frequency modes or other local oscillatory modes.

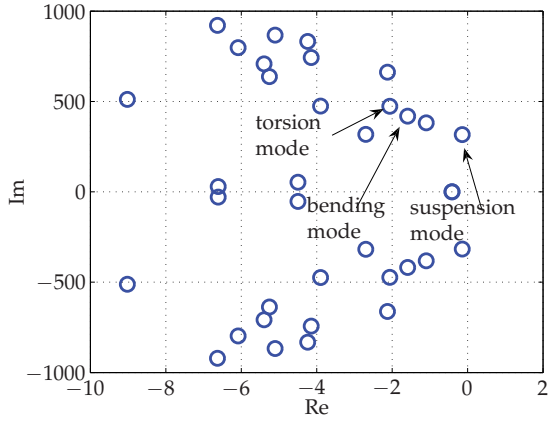

Fig. 27. Pole plot of the identified scaled metro car body (zoomed)

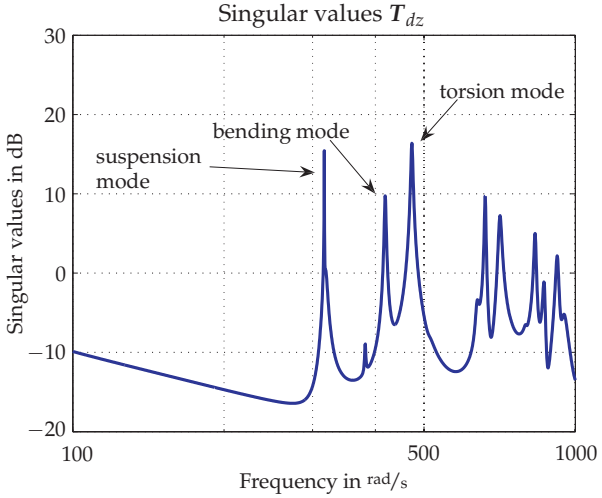

Fig. 28. Singular values of the identified scaled metro car body

The goal is to significantly dampen the torsional and the bending modes without destabilizing other oscillatory modes. For an objective evaluation of the active vibration control problem, the RMS of the frequency-filtered performance variables $z_{i,\text{ISO}}$ $(i = 1, \ldots, 6)$ are compared in the open-loop and closed-loop responses. These six performance quantities represent a quantification of passenger ride comfort. A more detailed analysis can be found in Kozek & Benatzky (2008) and Schirrer (2010).

3.4.2 LQG controller design

An LQG controller is designed for a reduced-order plant model with 28 states (the system is identified with 200 states, see Kozek et al. (2011)). Hence the system is transformed into a modal state space representation and all eigenmodes with an eigenfrequency higher than $f \approx 75\,\mathrm{Hz}$ are truncated and not considered for the controller design. The weighting functions for the regulator and the estimator design are

$$\boldsymbol{Q} = \begin{bmatrix} \mathbf{I}_{24\times 24} & \mathbf{0} \\ \mathbf{0} & 6\cdot 10^6 \cdot \mathbf{I}_{4\times 4} \end{bmatrix}, \qquad \boldsymbol{R} = \mathbf{I}_{2\times 2} \tag{33}$$

$$\boldsymbol{W} = 0.0054, \qquad \boldsymbol{V} = 2\cdot 10^{-4}\mathbf{I}_{2\times 2}. \tag{34}$$

Note that $\boldsymbol{Q}$ in (33) is chosen such that only the bending and the torsional vibrations should be significantly damped. A discussion of the results for the closed-loop system is given in Section 3.4.4.

3.4.3 $\mathcal{H}_2$ controller design

The $\mathcal{H}_2$ controller is designed for a plant model which only considers 3 eigenmodes (two of them describe the bending and torsional behaviour). For an efficient control design the frequency-dependent actuator and performance functions are specified as

$$\boldsymbol{W}_{\mathrm{act}} = G_{\mathrm{act}} \cdot \mathbf{I}_{2\times 2} = 188.5\cdot 10^9 \cdot \frac{(s^2 + 77.91s + 151800)^4}{(s+10000)^8} \cdot \mathbf{I}_{2\times 2}. \tag{35}$$

$$\boldsymbol{W}_{\mathrm{perf}} = G_{\mathrm{perf}} \cdot \mathbf{I}_{6\times 6} = \mathbf{I}_{6\times 6} \tag{36}$$

Note that the transmission zeros of $\boldsymbol{W}_{\mathrm{act}}$ are near the two target modes to be damped, causing the actuator action to be a maximum for these frequencies. A discussion of the results for the closed-loop system are given in Section 3.4.4.

3.4.4 Results

Table 5 and Figures 29, 30, 31, and 32 show the damping ability of both types of controllers. In both cases, the vibrations of the actively controlled system are significantly reduced compared to the open-loop response of the system. The accelerations at both ends of the structures, expressed by the performance variables z_1, z_2, z_5 and z_6 can be significantly reduced, whereas z_3 and z_4 are close to the open-loop response. This is explained due to the fact that the first torsional mode dominates the bending vibrations for the scale laboratory setup. For the LQG controller the singular values only differ for the torsional and the bending vibrations ($-14\,\mathrm{dB}$ and $-10\,\mathrm{dB}$). It is evident that only the eigenvalues of the two targeted flexible modes are affected by the controller. The unchanged mode at lower frequency is an almost uncontrollable suspension mode, while the higher flexible modes are not adversely affected by the control action.

Analogous results could be obtained using the frequency-weighed $\mathcal{H}_2$-optimal control design methodology: the achieved RMS reductions of the performance variables are approximately the same as for the LQG control method. Note that the bandwidth of the frequency-weighted controller is narrow around $f = 60 - 75\,\mathrm{Hz}$ where the actuator weightings are small. Contrary to the LQG approach, the target modes as well as other modes with a higher negative real part are positively influenced. This indicates that the model quality is sufficiently high and that

the control laws are insensitive to the occurring differences between design plant and actual system.

Performance position index i	1	2	3	4	5	6	avg.
RMS reduction $z_{i,\mathrm{ISO}}$ (LQG) in %	41.53	34.69	8.83	6.02	37.28	36.94	27.55
RMS reduction $z_{i,\mathrm{ISO}}$ ($\mathcal{H}_2$) in %	41.31	35.69	-4.00	4.59	34.89	36.16	24.77

Table 5. Laboratory testbed results: RMS reduction of the performance vector $\boldsymbol{z}$ by an LQG (system order 28) and an $\mathcal{H}_2$ controller (system order 23) utilizing strain feedback sensors

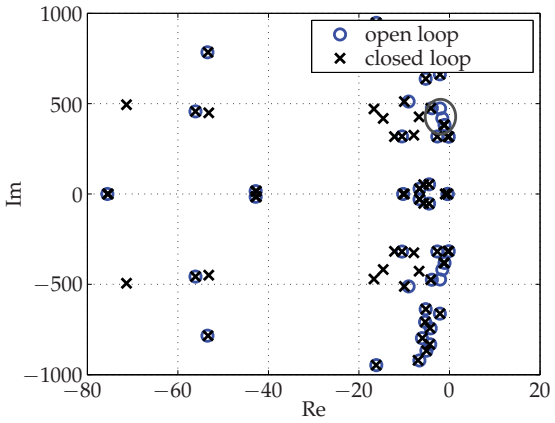

Fig. 29. Pole plot with/without LQG controller

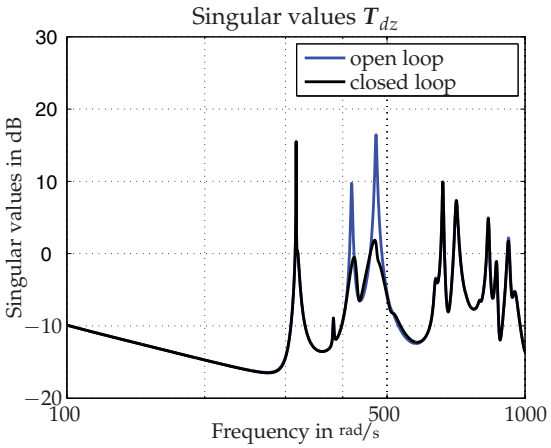

Fig. 30. Singular values of the frequency response plot with/without LQG controller

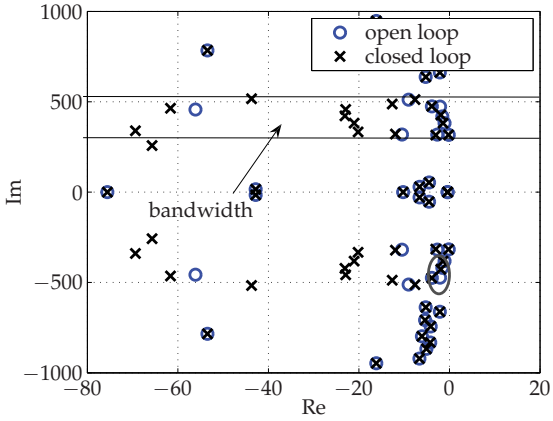

Fig. 31. Pole plot with/without $\mathcal{H}_2$ controller

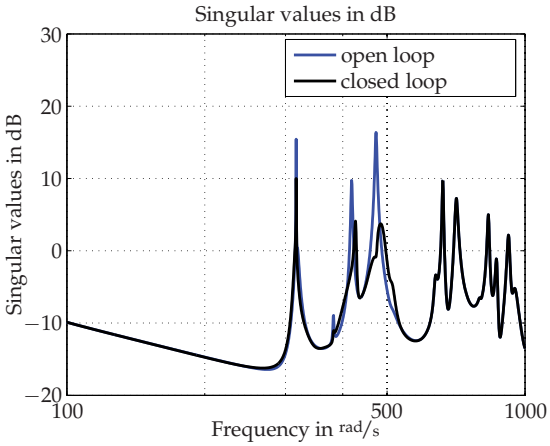

Fig. 32. Singular values of the frequency response plot with/without $\mathcal{H}_2$ controller

4. Conclusions

This chapter presents a case study on the design of MIMO control laws to reduce vibrations in a flexible metro rail car body and thus to improve passenger ride comfort. Direct structural actuation by Piezo actuators is considered and two sensor concepts – strain sensors (in a non-collocated setting) and acceleration sensors (collocated) – are evaluated. One part of the outlined studies focused on a simulation model of a full-size lightweight metro rail car body; the other part tests the control concepts on a laboratory testbed with a scale model of the car body. The control laws have been designed by LQG and by frequency-weighted $\mathcal{H}_2$-optimal control design methodologies. Both design methods are first studied in the simulation and compared. It is found that the weighted $\mathcal{H}_2$ designs yield controllers that perform satisfactorily in the presence of model uncertainty and independent of the sensor concept (strain sensors / non-collocation or acceleration sensors / collocation): the first three

modes of interest are significantly attenuated and the unknown modes in the high-frequency domain are hardly affected by the controller action, thus increasing the ride comfort for the passengers. The LQG controller minimizes the vibrations only for strain sensors in the non-collocated setup. Finally, both design methods, which have been studied for the lightweight rail car body simulations, are successfully implemented in a scaled laboratory setup: it is demonstrated that the target modes (torsion and bending) have been significantly damped by both controller types. A further advantage of the weighted $\mathcal{H}_2$ controller is that the controller action can be tuned for a specific bandwidth in the frequency domain, which is essential if the dynamics of the structure under consideration is uncertain or a control input is not desired for certain frequencies. The studies' results show the applicability of weighted $\mathcal{H}_2$ control for partially uncertain flexible-structure systems. The control goal of improving ride comfort is directly formulated as a weighted $\mathcal{H}_2$ minimization problem which justifies the presented study. However, a range of related publications show the design and application of robust $\mathcal{H}_\infty$-optimal controllers for this application, which can give robustness guarantees based on the structured singular value.

5. References

Benatzky, C. (2006). *Theoretical and experimental investigation of an active vibration damping concept for metro vehicles*, PhD thesis, Institute for Mechanics and Mechatronics, Division of Control and Process Automation, Vienna University of Technology, Austria.

Benatzky, C. & Kozek, M. (2005). Effects of local actuator action on the control of large flexible structures, *Proceedings of the 16th IFAC World Congress*, Prague, Chech Republic.

Benatzky, C. & Kozek, M. (2007a). An actuator fault detection concept for active vibration control of a heavy metro vehicle, *Proceedings of the 14th International Congress on Sound and Vibration (ICSV14), Cairns, Australia*.

Benatzky, C. & Kozek, M. (2007b). An identification procedure for a scaled metro vehicle - flexible structure experiment, *Proceedings of the European Control Conference ECC 2007, Kos, Greece*, Kos, Greece.

Benatzky, C., Kozek, M. & Bilik, C. (2006). Experimental control of a flexible beam using a stack-bending-actuator principle, *Proceedings of the 20th Scientific Conference*, Hanoi, Vietnam.

Benatzky, C., Kozek, M. & Jörgl, H. (2007). Comparison of controller design methods for a scaled metro vehicle - flexible structure experiment, *Proceedings of the 26th American Control Conference, New York, USA*.

Bilik, C. (2006). *Aufbau und Inbetriebnahme des Prüfstandmodelles eines Schienenfahrzeug-Wagenkastens zum Nachweis von aktiver Schwingungsdämpfung*, Diploma thesis, Vienna University of Technology, Vienna.

Bilik, C., Benatzky, C. & Kozek, M. (2006). A PC-based multipurpose test bed environment for structural testing and control, *Proceedings of the 3rd International Symposium on Remote Engineering and Virtual Instrumentation*, Maribor, Slovenia.

Foo, E. & Goodall, R. M. (2000). Active suspension control of flexible-bodied railway vehicles using electro-hydraulic and electro-magnetic actuators, *Control Engineering Practice* 8(5): 507–518.

Frederich, F. (1984). *Die Gleislage - aus fahrzeugtechnischer Sicht*, Vol. 108 (12) of *Gleislauftechnik*, Siemens Verlagsbuchhandlung, pp. 355 – 361.

Gawronski, W. (2004). *Advanced structural dynamics and active control of structures*, Springer, New York.

Hansson, J., Takano, M., Takigami, T., Tomioka, T. & Suzuki, Y. (2004). Vibration Suppression of Railway Car Body with Piezoelectric Elements, *JSME International Journal Series C* 47(2): 451–456.

ISO (1997). ISO2631-1: Mechanical vibration and shock - evaluation of human exposure to whole-body vibration. Part 1: General requirements, International Organization for Standardization. Corrected and reprinted July 15th, 2007.

Kamada, T., Tohtake, T., Aiba, T. & Nagai, M. (2005). Active vibration control of the railway vehicle by smart structure concept, *in* S. Bruni & G. Mastinu (eds), *19th IAVSD Symposium - Poster Papers*.

Kozek, M. & Benatzky, C. (2008). Ein maßstäbliches Experiment zur aktiven Schwingungsdämpfung eines Eisenbahn-Wagenkastens, *at - Automatisierungstechnik* 10(56): 504–512.

Kozek, M., Benatzky, C., Schirrer, A. & Stribersky, A. (2011). Vibration damping of a flexible car body structure using piezo-stack actuators, *Control Engineering Practice* 19(3): 298 – 310. Special Section: IFAC World Congress Application Paper Prize Papers.
URL: *http://www.sciencedirect.com/science/article/B6V2H-4X3MR4Y-2/2/3ef1d868e70c2b6f10fd9412f9c8c1de*

Luenberger, D. G. (1964). Observing the state of a linear system, *IEEE Transactions on Military Electronics* 8(2): 74–80.

Mohinder, S. & Angus, P. (2001). *Kalman Filtering: Theory and Practice Using MATLAB*, Wiley Interscience, John Wiley & Sons, USA.

Popprath, S., Benatzky, C., Bilik, C., Kozek, M., Stribersky, A. & Wassermann, J. (2006). Experimental modal analysis of a scaled car body for metro vehicles, *Proceedings of the 13th International Congress on Sound and Vibration (ICSV13), Vienna, Austria*.

Popprath, S., Schirrer, A., Benatzky, C., Kozek, M. & Wassermann, J. (2007). Experimental modal analysis of an actively controlled scaled metro vehicle car body, *Proceedings of the 14th International Congress on Sound and Vibration (ICSV14), Cairns, Australia*.

Preumont, A. (2006). *Mechatronics: Dynamics of Electromechanical and Piezoelectric Systems*, Springer.

Schandl, G. (2005). *Methodenuntersuchung zur aktiven Schwingungsreduktion eines Schienenfahrzeugwagenkastens*, PhD thesis, Vienna University of Technology, Vienna.

Schandl, G., Lugner, P., Benatzky, C., Kozek, M. & Stribersky, A. (2007). Comfort enhancement by an active vibration reduction system for a flexible railway car body, *Vehicle System Dynamics* 45(9): 835–847.

Schöftner, J. (2006). *Aktive Schwingungsdämpfung eines Schienenfahrzeugwagenkastens durch $\mathcal{H}_2$-Regelung*, Master's thesis, Institute for Mechanics and Mechatronics, Division of Control and Process Automation, Vienna University of Technology.

Schirrer, A. (2010). *Co-Simulation of Rail Car Body Vibration Control with SimPACK®*, VDM Verlag Dr. Müller, Saarbrücken, Germany.

Schirrer, A. & Kozek, M. (2008). Co-simulation as effective method for flexible structure vibration control design validation and optimization, *Control and Automation, 2008 16th Mediterranean Conference on*, pp. 481 –486.

Schirrer, A., Kozek, M. & Benatzky, C. (2008). Piezo stack actuators in flexible structures: Experimental verification of a nonlinear modeling and identification approach, *6th EUROMECH Nonlinear Dynamics Conference (ENOC 2008), OPEN-ACCESS library*. URL: *http://lib.physcon.ru*

Schirrer, A., Kozek, M., Plank, A., Neumann, M., Badshah, S. & Wassermann, J. (2008). Vibration analysis of an actively controlled flexible structure using speckle interferometry, *Proceedings of 15th International Congress on Sound and Vibration (ICSV15)*.

Skogestad, S. & Postlethwaite, I. (1996). *Multivariable feedback control*, John Wiley & Sons.

Stribersky, A., Müller, H. & Rath, B. (1998). The development of an integrated suspension control technology for passenger trains, *Proceedings of the Institution of Mechanical Engineers, Part F: Journal of Rail and Rapid Transit*, Vol. 212, pp. 33–42.